Flow over seal whiskers: significance of geometric features on force and frequency response

Kathleen Lyons

Department of Engineering Physics, University of Wisconsin–Madison, Madison WI

Christin T. Murphy

Naval Undersea Warfare Center, Newport RI

Jennifer A. Franck

Department of Engineering Physics, University of Wisconsin–Madison, Madison WI

Abstract. The complex undulated geometry of seal whiskers has been shown to significantly modify the turbulent structures directly downstream, resulting in a reduction of hydrodynamic forces as well as modified vortex-induced-vibration response when compared with smooth whiskers. Although the unique hydrodynamic response has been well documented, an understanding of the fluid flow effects from each geometric feature remains incomplete. In this computational investigation, non-dimensional geometric parameters of the seal whisker topology are defined in terms of their hydrodynamic relevance, such that wavelength, aspect ratio, undulation amplitudes, symmetry and undulation off-set can be varied independently of one another. A two-factor fractional factorial design of experiments is used to create 16 unique geometries, each of which dramatically amplifies or attenuates the geometric parameters compared with the baseline model. The flow over each unique topology is computed with a large-eddy simulation at a Reynolds number of 500 and the effects on force and frequency are recorded. The results determine the specific fluid flow impact of each geometric feature which will inform both biologists and engineers who seek to understand the impact of whisker morphology or lay out a framework for biomimetic design of undulated structures.

1. Introduction

Harbor seals, among other seal species, demonstrate incredible hydrodynamic tracking abilities facilitated by the three-dimensional undulated geometry of their whiskers [1]. The undulated topology is shown to significantly reduce hydrodynamic forces as well as modify the vortex-induced-vibration (VIV) response when compared to smooth whiskers [2]. Understanding the complex fluid dynamics and frequency response of whisker undulations will aid in understanding the impact of seals' specialized whisker morphology, and help provide context for differences observed between species. Furthermore, biomimetic inspiration from the whisker undulations could impact a multitude of engineering designs that seek to minimize vortex-induced-vibration (VIV), reduce drag, or disrupt the frequency response in a large variety of structures.

The tracking performance of seal whiskers is well documented through a series of hydrodynamic-trail following exercises of a trained blind-folded seal [1, 3]. Through these experiments, it is shown that harbor seals can detect flow disturbances with their whiskers, even those generated over long distances. Additionally, seals are shown to distinguish between disturbances left by objects of different sizes and shapes [4], demonstrating that they can use their whiskers to discriminate among specific flow signatures, and likely among various prey types. To complement the hydrodynamic tracking experiments, systematic exploration of the whisker system's tactile sensitivity in a live seal reveals the ability to detect flow perturbations on the order of 1 mm/s, approximately three orders of magnitude smaller than their swimming speed of 1 m/s [5]. In controlled laboratory flume experiments, excised seal whiskers exhibit a broad range of frequency response in water flow with amplitudes significantly influenced by the angle of attack, or orientation of the whisker, with respect to the freestream flow [6, 7].

The advanced tracking ability of the seal is attributed in part to the unique morphology of its whiskers, modeled in figure 1a. Results from a combination of experimental particle-image velocimetry (PIV) and computational fluid dynamics (CFD) experiments show that the spanwise undulations of the seal whisker model disrupt the strong von Kármán vortex street that is characteristic of smooth cylinders, thus modifying the downstream vortical structures and resulting forces [2]. This study, among others, demonstrates effective suppression of VIV in the seal whisker model. As shown in figure 1b, the regular shedding pattern of low pressure, alternating sign vortices on a smooth elliptical cylinder is replaced with a complex structure of intertwined vorticity when the seal whisker undulations are added. These flow structures create a higher pressure region immediately downstream, significantly reducing drag force and lift force oscillations as well as shortening the mean recirculation length.

The whisker model in figure 1a has continued to be explored both computationally and experimentally. At $Re = 1800$, a direct comparison to an elliptical cylinder and a simple wavy cylinder is performed experimentally, where dynamic mode decomposition of the flow field indicates strong disruption of the energy redistribution process

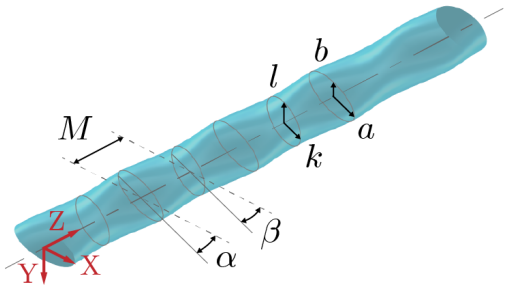

(a) Isometric view of baseline seal whisker model created from two different sized ellipses a distance M apart, major axes a and k, minor axes b and l, inclined at incident angles α and β with respect to the x-axis.

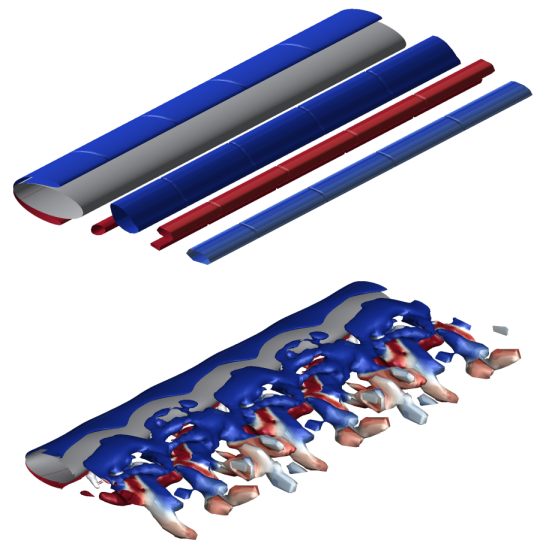

(b) Flow over a smooth ellipse (top) compared with the flow over the seal whisker model (bottom) reveal significantly different flow structures and hydrodynamic response as a result of the undulations.

Figure 1: Geometric parameters of the baseline model as originally defined by Hanke et al. [2] creates two coordinating sets of spanwise undulations along the z-axis, significantly affecting the force response and flow structures.

immediately downstream of the whisker [8], which varies with respect to angle of attack [9, 10]. The drag reduction properties are further confirmed computationally via a lattice Boltzmann method, in which a hydrodynamic disturbance is created via an upstream paddle to assess the whisker's response to stimulation [11].

The whisker model described above is constructed from average measurements of digital photography from 13 adult harbor seal whiskers, which exhibit significant variation in some geometric parameters, specifically the angles of incidence α and β [12]. A follow-up investigation by Rinehart et al. [13] performs independent whisker characterization using 27 whiskers from harbor and elephant seals. Among the findings are smaller mean angles of incidence, α and β, of 0.303 and 1.079 degrees respectively, in contrast with the larger angles presented by Hanke et al. of $\alpha = 15.27$ degrees and $\beta = 17.60$ degrees. However, both investigations note the large statistical variability in the angles, which directly affect the amplitude of the undulations on the seal whisker. Research on the fluid flow over whisker models has varied in the representation of the angles of incidence with some research claiming they are relatively unimportant features [14] and others setting the angles of incidence to zero [12, 15]. In addition to the aforementioned models primarily built from harbor seals and elephant seals, morphological analyses report geometric variation both within and between species [16, 17].

The statistical variation found in nature highlights the relevance of exploring the hydrodynamic effects of geometric variation in the seal whisker morphology. The model parameters proposed by Hanke et al. are most prevalent in the literature, however, a handful of geometry variations are explored computationally. Witte et al. explore two variations that indicate a larger wavelength has a slightly decreased root-mean-square lift force but the same mean drag force [12]. Hans et al. explore four different geometric models and demonstrate that both coordinate directions of undulation amplitudes are necessary for maximum drag-reduction benefits, however, the angle of incidence has only a weak influence on drag [14]. In a recent work, Liu et al. [15] investigate a geometric model based on model parameters of Rinehart et al. [13]. Results indicate that the undulations in opposing directions must alternate with one another along the span of the seal whisker for optimal hydrodynamic force reduction. By modifying the amplitude and wavelength, it is seen that the whisker topology suppresses lift oscillation over a wide range of parameters.

Without systematic and significant variations in undulation morphology, it remains unclear which geometric features or combinations of features are most important, and how specific features correlate with force reduction and frequency response. The goal of this paper is to isolate the main geometric features of the seal whisker model in terms of their hydrodynamic relevance. First, new geometric parameters are defined that are non-dimensional and independent of one another to enable systematic variation. Each of these parameters is varied dramatically from the baseline model, beyond the range of what is biologically found in seals. By intensifying and modifying the geometric features, their effects and interactions are more readily observed, and a better understanding of their contribution to drag reduction, root-mean-square lift reduction, and frequency response modification can be achieved.

The parametric study of various morphological features is performed computationally with a large-eddy simulation (LES). It is accomplished through a two-factor fractional factorial design of experiments that determines a 16 simulation test matrix of various seal whisker topologies, each with geometry modifications derived from the model proposed by Hanke et al. [2]. The resulting time-averaged forces and frequency spectra are recorded, as well as velocity contours and streamlines at various spanwise locations along the whisker model. The following section will describe the modifications of the geometric features and detail the computational methods. The results and discussion will highlight the important geometric features and two-feature combinations that most significantly affect the forces and frequency and then discuss the resulting flow structures and downstream flow characteristics.

2. Methods

2.1. Geometric Parameters

The seal whisker model geometry in figure 1a is defined by seven geometric parameters. Four parameters govern the major and minor axes of two ellipses (a, b, k, and l), two identify the angle of incidence of each ellipse (α and β) and the last parameter specifies the distance between the ellipses, M, which is half of the undulation wavelength. Although these parameters are convenient for constructing the model, it is difficult to make systematic variations and isolate the effects of the major/minor axis lengths and angles of incidence as both of these parameters influence the undulation amplitudes. Thus, using the same model, the geometric parameters are redefined in figure 2. A summary of the new geometric descriptions and their nondimensionalization is given in table 1.

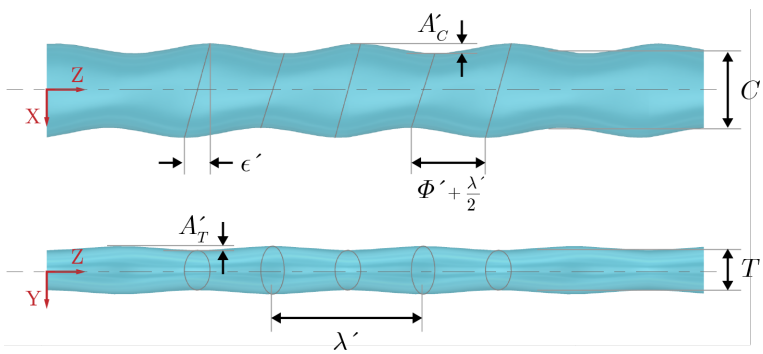

Figure 2: Schematic of the baseline undulated whisker geometry and the hydrodynamic-based geometric parameters that define the undulation features as described in table 1. Top view (top panel) and front view (bottom panel), where flow is along the positive x-axis.

Table 1: The description of the undulated geometric features shown in figure 2 and the correspondence between those previously defined by Hanke et al. [2] (shown in figure 1a).

Nondimensional parameter	**Hydrodynamic description**	**Derivation from previous parameters**
T	mean thickness	$T = b + l$
$\gamma = C/T$	aspect ratio	$C = a\cos\alpha + k\cos\beta$
$\lambda = \lambda'/T$	nondimensional wavelength	$\lambda' = 2M$
$A_T = A_T'/T$	transverse amplitude	$A_T' = \lvert b - l\rvert$
$A_C = A_C'/T$	streamwise amplitude	$A_C' = \lvert a\cos\alpha - k\cos\beta\rvert$
$\epsilon = 2\epsilon'/\lambda'$	undulation offset	$\epsilon' = \lvert 2a\sin\alpha\rvert$
$\phi = 2\phi'/\lambda'$	undulation symmetry	$\phi' = \lvert k\sin\beta - a\sin\alpha\rvert$

Defining freestream flow in the positive x-axis and following aerodynamic convention, the two major length parameters in figure 2 are the mean thickness, T, and the mean chord length, C. The aspect ratio, or slenderness, of the geometry, is defined as $\gamma = C/T$. The amplitudes of undulations in thickness and chord length are described by A_T and A_C respectively. The periodic occurrence of both the chord and thickness undulations is defined by a single wavelength, λ. The wavelength and amplitudes are nondimensionalized by the mean thickness, T.

The undulation offset, ϵ, controls the alignment of undulation peaks along the leading and trailing edges, as measured in the x-z plane of figure 2. When $\epsilon = 0$, the peak amplitudes from leading to trailing edge are aligned with the x-axis. The undulation symmetry, ϕ, defines the steepness, or bias, of the undulation. The dimensional value of ϕ' is best represented in the x-z plane in figure 2 where it depicts the distance by which the trough of the undulation has been shifted, or biased. When $\phi = 0$, the undulations along the leading and trailing edges are exactly sinusoidal. The undulation offset and symmetry parameters are nondimensionalized by the half-wavelength, $\lambda'/2$.

2.2. Experimental Approach

Using a two-parameter fractional factorial design, similar to the design structure used by Jung et al. [18], a matrix of simulations is constructed to independently test the influence of each geometric parameter. The parameter values outlined in Hanke et al. [2] represent the baseline dimensions for the analysis, hereafter referred to as the *baseline model*. These values are used throughout the literature as representative values for the seal whisker geometry [19, 14, 20, 11, 8, 10, 9]. In order to understand the effects of each nondimensional parameter, values above and below the baseline value are outlined in table 2. A total of 16 simulations are performed with a specific combination of the low (-1) and high (1) values. The resulting test matrix, informed by the fractional factorial design of experiments, is designed as a screening test of specific combinations that systematically reduces the number of cases required to determine the most significant variables [21, 22]. Using this combination of simulations, the geometric parameters and two-parameter interactions that most strongly influenced the drag, the root-mean-square lift, and the dominant frequency response are identified and ranked by importance.

Table 2: The low and high values used to vary each of the geometric parameters compared to the baseline values commonly used in literature. The full matrix of simulations is described in detail in table 4.

	$\boldsymbol{\lambda}$	$\boldsymbol{\gamma}$	$\boldsymbol{A_T}$	$\boldsymbol{A_C}$	$\boldsymbol{\epsilon}$	$\boldsymbol{\phi}$
Low (-1)	1.8	1.0	0.05	0.05	0.20	0
Baseline (0)	3.4	1.9	0.09	0.23	0.34	0.015
High (1)	5.0	3.0	0.30	0.30	0.60	0.300

To amplify the effect on the response variables, geometric high and low values are

chosen to span a wide range of deviation from the baseline model. Values of λ are influenced by previous research on wavy cylinders that show an increase in forces when $\lambda/D_m < 2$, where D_m is the mean diameter [23]. Therefore, the low value was chosen to be $\lambda = 1.8$ and the high value at an equal $\Delta\lambda$ above the baseline at $\lambda = 5$. The aspect ratio ranges from a circular cross section ($\gamma = 1$) to an elliptical cross-section of $\gamma = 3$, again maintaining approximately the same $\Delta\gamma$ in each direction from the baseline value. The amplitudes, A_T and A_C, have low values of 0.05, or 5% of the thickness, such that they are small but nonzero. The high value of both amplitudes is 0.3, or 30% of the thickness, which represent significant undulations. The low value of ϕ is zero, representing perfectly symmetrical undulations, whereas the high value is 0.30, or a 30% bias in the undulation symmetry. The low value of the undulation offset is $\epsilon = 0.2$ to allow for a ϕ value of zero to be reached for all configurations. The high ϵ value is 0.6, representing a very noticeable phase difference between the undulations on the leading and trailing edges.

The effects of each geometric parameter are assessed with three response variables. The drag and lift coefficients are computed as,

$$C_D = \frac{2F_D}{\rho U_\infty^2 T L_z} \tag{1}$$

and

$$C_L = \frac{2F_L}{\rho U_\infty^2 C L_z}, \tag{2}$$

where L_z is the span length in the z-direction. Drag is normalized by the averaged frontal area, TL_z, and lift is nondimensionalized by the planform area, CL_z. Due to the lack of camber in all models the mean C_L is nominally zero, and thus the mean drag coefficient, $\overline{C_D}$, and the root-mean-square (RMS) value of the lift oscillations, $C_{L,RMS}$ are reported as response variables. The frequency response is obtained from the oscillating lift coefficient, and is nondimensionalized as

$$f^* = \frac{f D_h}{U_\infty} \tag{3}$$

where D_h is the average hydraulic diameter of the model calculated in the same manner as Witte et al. [12]. The response variable is the Strouhal number (St), which is defined in this context to be the nondimensional frequency with the strongest response peak.

The average effect of each parameter on the response variable is calculated by computing the difference between the average of the response to the parameter at the high level and the average of the response to the parameter at the low level [21, 22]. The average effect of a parameter A on the response variable $\overline{C_D}$ is

$$E_A = \left[\frac{1}{n/2}\sum_{k=1}^{n/2} \overline{C_D}^k\right]_{A^+} - \left[\frac{1}{n/2}\sum_{k=1}^{n/2} \overline{C_D}^k\right]_{A^-} \tag{4}$$

where A^- represents all cases with a low value of A and A^+ represents all cases with a high value. For a matrix of $n = 16$ simulations, the response variable output for the kth

simulation is given by $\overline{C_D}^k$. The effect of two-way interactions of geometric parameters, defined as A^*B, is similarly

$$E_{A^*B} = \frac{1}{2}\left(\left[\frac{1}{n/4}\sum_{k=1}^{n/4}\overline{C_D}^k\right]_{A^+B^+} - \left[\frac{1}{n/4}\sum_{k=1}^{n/4}\overline{C_D}^k\right]_{A^-B^+}\right) - \frac{1}{2}\left(\left[\frac{1}{n/4}\sum_{k=1}^{n/4}\overline{C_D}^k\right]_{A^+B^-} - \left[\frac{1}{n/4}\sum_{k=1}^{n/4}\overline{C_D}^k\right]_{A^-B^-}\right). \tag{5}$$

2.3. Computational Details

An incompressible large-eddy simulation (LES) is used to perform the simulations. The sub-grid scale stresses are calculated with a constant Smagorinsky model [24]. The governing equations are solved using OpenFOAM libraries [25] that utilize a second-order accurate finite-volume scheme.

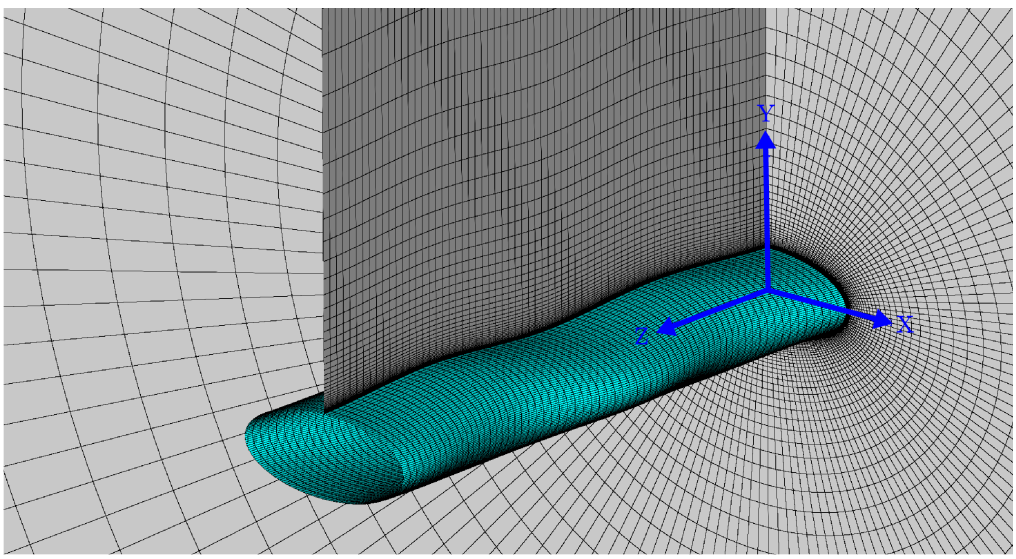

Figure 3: Mesh for the LES simulation of the baseline model at $Re_{D_h} = 640$ (equivalent to $Re_T = 500$). Mesh details are listed in table 3.

In order to sweep through a large matrix of 16 different three-dimensional geometries, much care is taken to reduce the computational cost yet still maintain an accurate description of the salient features of the geometry, particularly in terms of properly resolving the response variables $\overline{C_D}$, $C_{L,RMS}$, and St. The final mesh for the baseline model is depicted in figure 3, and contains 160 points in the circumferential direction, 68 points in the radial direction, and 68 points in the spanwise direction. The outer domain is circular, and is $75T$ away from the centered body. Two periodic wavelengths are simulated in the spanwise direction. The final mesh selection for the baseline model produces results that compare favorably with a high resolution direct numerical simulation (DNS), detailed in the supplemental information along with a more detailed analysis of the mesh sensitivity.

The simulations for the 16 variations in seal whisker topology are run at a Reynolds number, $Re_T = U_\infty T/\nu$, of 500. The geometry parameters are non-dimensionalized with respect to thickness, which makes it a consistent choice for the Reynolds number. However, others have computed simulations based on hydraulic diameter, D_h, thus additional simulations are performed to directly compare results at $Re_{D_h} = 500$. These results show good agreement in terms of the response parameters of C_D, $C_{L,RMS}$ and St, the details of which are presented in the supplemental information.

The meshes for the remaining 16 simulations follow similar trends as that for the baseline model, however modifications are made to account for the two different aspect ratios (circular and elliptical), and for the two different wavelengths that modify the total spanwise domain of the simulation (long and short). The mesh characteristics for each of these categories are given in table 3. There are three cases (CS3, ES2, ES4) in which additional mesh points are added to account for highly complex geometries.

Table 3: Mesh variation by geometry characteristics. Additional mesh points are added to specific models (CS3, ES2, ES4) within these categories due to increased geometrical complexity.

Class	$\boldsymbol{N}$	$\boldsymbol{L_z = 2\lambda}$	$\boldsymbol{\gamma}$	$\boldsymbol{\lambda}$	$\boldsymbol{N_z}$	$\boldsymbol{N_\theta}$	$\boldsymbol{N_r}$	$\boldsymbol{\Delta z}$
Circular Short (CS)	0.718M	3.6	1.0	1.8	68	160	68	0.054
Elliptical Short (ES)	1.01M	3.6	3.0	1.8	68	224	68	0.054
Circular Long (CL)	1.08M	10.0	1.0	5.0	102	160	68	0.100
Elliptical Long (EL)	1.52M	10.0	3.0	5.0	102	224	68	0.100

3. Results and Flow Physics

3.1. Identifying Dominant Geometric Parameters

The results of all 16 geometry modifications in terms of the value of each of the response variables are tabulated in table 4. Each row also contains the combination of low (-1) and high (1) geometry modifications for the specific configuration (see table 2). The average effects of the geometric parameters on each response variable are calculated using equations 4 and 5 and displayed in the Pareto charts in figure 4.

The Pareto charts rank the effects for each of the three response variables. Most important to the screening test is the overall ranking of effects and not the absolute effect magnitude, however the direction of correlation is indicated by the shading of red (positive correlation) or gray (negative correlation). Interacting parameters have a larger influence together than either does individually, however not every combination of two-parameter interaction is captured since the cumulative effects of multiple two-way interactions are measured simultaneously and each effect cannot be extracted individually, leaving the two-way interactions confounded with one another [22, 21].

Table 4: Measured response variables by model and geometric variation. See table 2 for specific geometric values of each variation. Models are grouped by class: Circular Short (CS), Elliptical Short (ES), Circular Long (CL), Elliptical Long (EL).

Model	$\overline{C_D}$	$C_{L,RMS}$	St	γ	λ	A_C	A_T	ϵ	ϕ
Baseline	0.715	0.016	0.20	0	0	0	0	0	0
CS1	1.17	0.311	0.21	-1	-1	-1	-1	-1	-1
CS2	1.11	0.100	0.21	-1	-1	-1	1	-1	1
CS3	1.04	0.036	0.23	-1	-1	1	-1	1	1
CS4	1.04	0.038	0.17	-1	-1	1	1	1	-1
CL1	1.05	0.075	0.22	-1	1	-1	-1	1	-1
CL2	1.10	0.057	0.18	-1	1	-1	1	1	1
CL3	1.05	0.052	0.20	-1	1	1	-1	-1	1
CL4	1.02	0.037	0.12	-1	1	1	1	-1	-1
ES1	0.657	0.051	0.35	1	-1	-1	-1	1	1
ES2	0.668	0.028	0.35	1	-1	-1	1	1	-1
ES3	0.655	0.044	0.33	1	-1	1	-1	-1	-1
ES4	0.667	0.020	0.34	1	-1	1	1	-1	1
EL1	0.635	0.023	0.36	1	1	-1	-1	-1	1
EL2	0.633	0.008	0.22	1	1	-1	1	-1	-1
EL3	0.634	0.017	0.36	1	1	1	-1	1	-1
EL4	0.611	0.003	0.23	1	1	1	1	1	1

However, the test matrix is specifically designed to capture the λ and γ interactions reported in figure 4.

Figure 4 shows that the parameters with the largest effect on the response variables are γ, A_C, A_T, and λ. The two-way interactions $\lambda^*\epsilon$ and λ^*A_T are also shown to be significant. In terms of single parameters, the undulation offset, ϵ, and the undulation symmetry, ϕ, are the least significant. Comparing the response variables to one another, there are more parameters that significantly affect $C_{L,RMS}$ in contrast to the fewer influential parameters for $\overline{C_D}$. As $C_{L,RMS}$ is a measure of an oscillating component, it may be more sensitive to changes in geometric parameters than a mean value such as C_D. However, the most important factors affecting $C_{L,RMS}$ are the same as those influencing $\overline{C_D}$, that is γ, A_C, and λ, although, the relative effect of γ is smaller with respect to $C_{L,RMS}$ than in the $\overline{C_D}$ response.

Although γ is the highest ranking parameter on all of the Pareto charts, its strong effect on the response parameters is not surprising as the influence of aspect ratio is well known in aerodynamics. The high and low values of γ distinguish between the two classes of geometries tested, those with a baseline circular aspect ratio and those with a streamlined elliptical aspect ratio. The other undulation parameters can be applied to

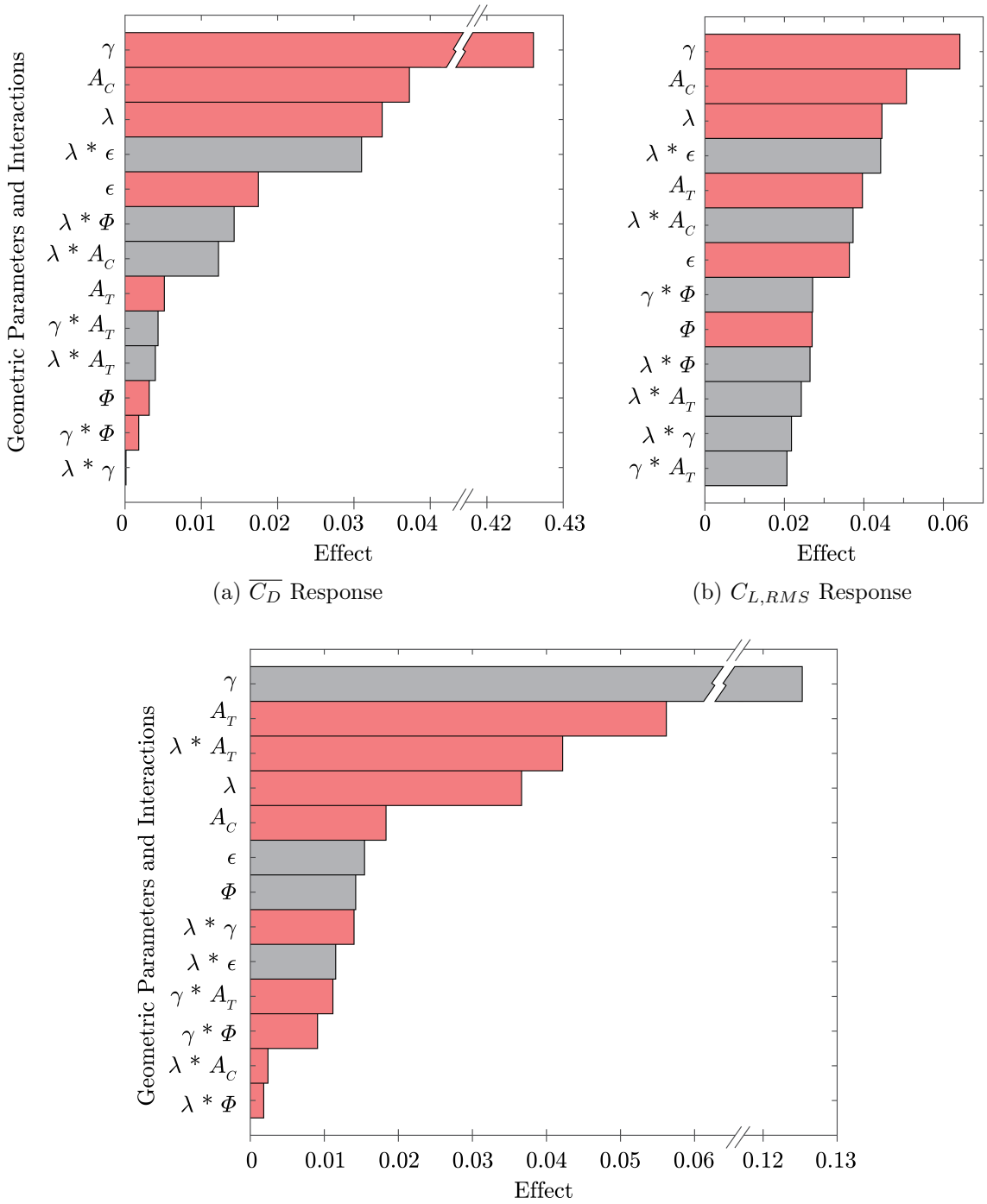

(a) $\overline{C_D}$ Response

(b) $C_{L,RMS}$ Response

(c) St Response

Figure 4: Pareto charts summarizing the effects of modifications to geometric parameters on three response variables. Gray shaded regions indicate a positive correlation and the red shaded regions indicate a negative correlation. γ, A_C, A_T, and λ are seen to have the largest effects.

each of these regimes, and their impacts are discussed below by identifying simulations with high and low parameter values within a specific aspect ratio class.

3.2. Effect of A_T

To analyze the effect of a change in thickness amplitude, A_T, two similar geometries with varying A_T attributes are compared in figure 5, with EL1 (low A_T) in figure 5a and EL2 (high A_T) in figure 5b. The two geometries have a similar C_D, however, the high undulation amplitude of EL2 reduces the $C_{L,RMS}$ by 66%.

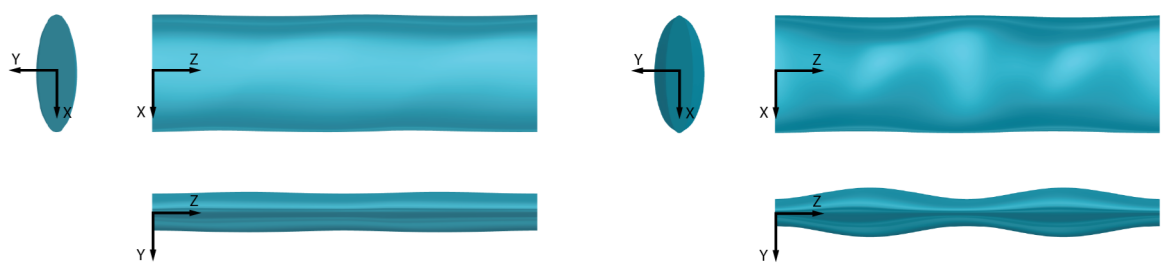

(a) EL1 (low A_T) (b) EL2 (high A_T)

Figure 5: Directly comparing a low A_T and high A_T model with three views: top view in the x-z plane, front view in the y-z plane, and side view in the x-y plane. Flow is along the positive x-axis.

The time-averaged streamwise velocity contours in figure 6a show significant differences between the two geometries. The recirculation length across the peak and trough locations are nearly constant for EL1, whereas they vary dramatically across the span for EL2. EL2 has significant flow reversal at peak thickness in contrast to the trough location where the recirculation length is dramatically reduced due to a locally reduced frontal area. The streamlines in figure 6b also show little to no recirculation immediately downstream of the trough cross-section of EL2 and high spanwise velocities downstream of the peaks. The lack of a uniform velocity profile between peak and trough regions promotes spanwise momentum transport and results in the vortex break up shown in figure 6c, which displays isosurfaces of the Q-criterion colored by magnitude of spanwise vorticity.

Figure 7 displays the C_L frequency spectra for EL1 and EL2 compared with a smooth elliptical cylinder of the same aspect ratio. The EL1 (low A_T) and cylinder spectra show a similarity in shape and peak value around $f^* = 0.35$. EL1 also has a secondary peak around $f^* = 0.22$ not present for the smooth cylinder. At high A_T, the $f^* = 0.35$ peak is attenuated and the $f^* = 0.22$ peak becomes dominant. The attenuation in the $f^* = 0.35$ peak leads to a lower overall signal magnitude evident in the strong reduction of $C_{L,RMS}$ for high A_T. The difference in dominant shedding frequencies is likely due to the change in development, growth, and shedding of the

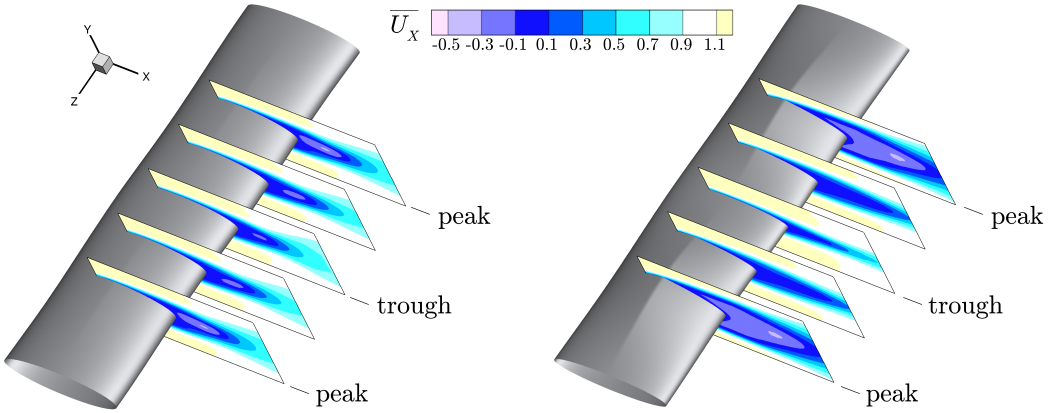

(a) The comparison of time-averaged streamwise velocity contours for low A_T (left) and high A_T (right) models shows significant variation between recirculation length at peak and trough cross sections. Contours are shown at equally spaced spanwise locations where peak and trough correspond to A_T undulations.

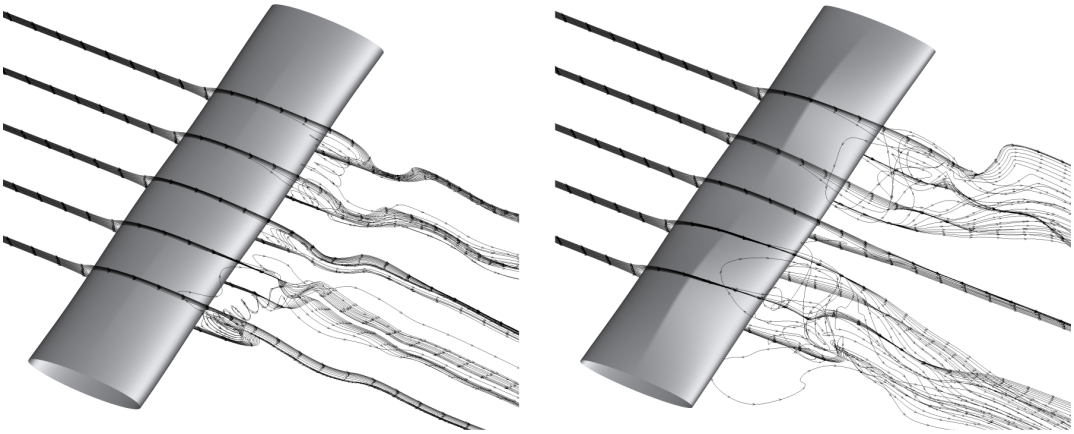

(b) Velocity streamlines at peak and trough spanwise locations denoted in 6a demonstrate more spanwise transport for the high A_T model.

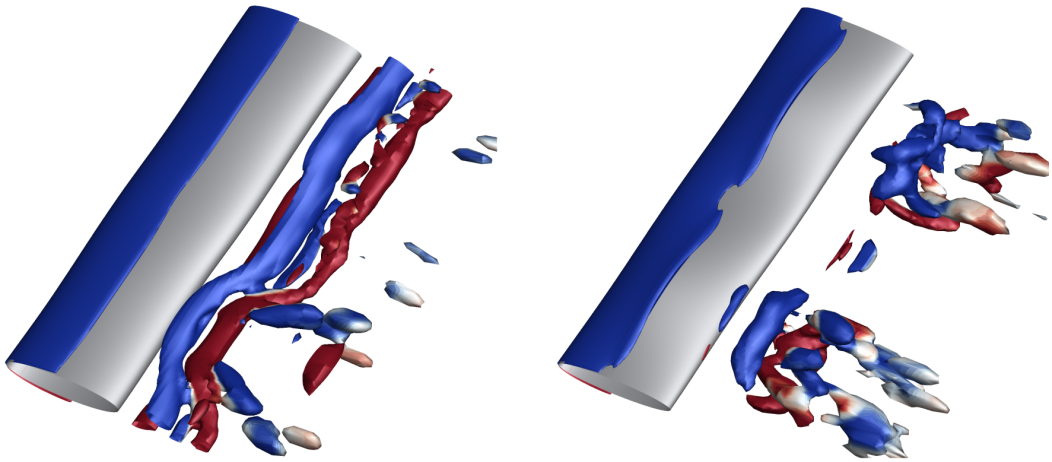

(c) Isosurfaces of Q-criterion colored by spanwise vorticity display long, coherent structures at low A_T and breakup at high A_T.

Figure 6: Flow comparison between low and high A_T geometries. EL1 (low A_T) in the left column, EL2 (high A_T) in the right column.

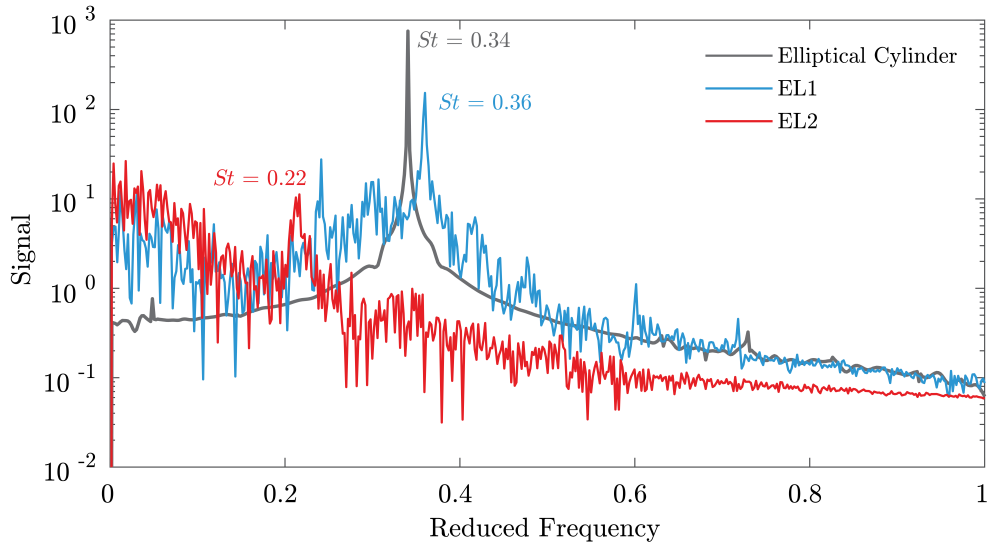

Figure 7: C_L spectra for the EL1 (low A_T) and EL2 (high A_T) geometries shown in figure 5 directly compared with a smooth elliptical cylinder. The EL1 frequency spectrum shows a spectra more similar to the cylindrical case while the EL2 response is smaller in magnitude with a peak at lower frequency.

differently sized and shaped spanwise structures as indicated in the isosurfaces in figure 6c.

3.3. Effect of A_C

The effect of the chord length amplitude, A_C, is shown by comparing the flow over models CL2 (low A_C) and CL4 (high A_C) in figure 8. These two geometries both have high A_T, high λ, and a circular aspect ratio. As A_C is increased, the response parameters show a 7% reduction in $\overline{C_D}$ and a 35% decrease in $C_{L,RMS}$.

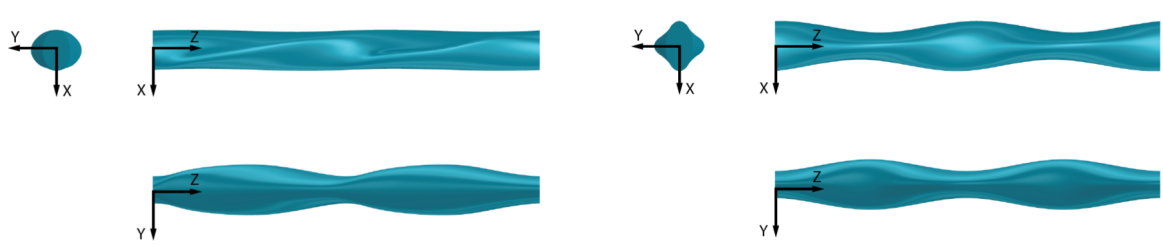

(a) CL2 (low A_C) (b) CL4 (high A_C)

Figure 8: Directly comparing a low A_C and high A_C model with three views in the same configuration as figure 5.

Contour plots of the mean streamwise velocity and associated streamlines are shown in figures 9a and 9b. Along the span, both models have a similar pattern of increasing and decreasing recirculation lengths, primarily the result of their similarly high A_T

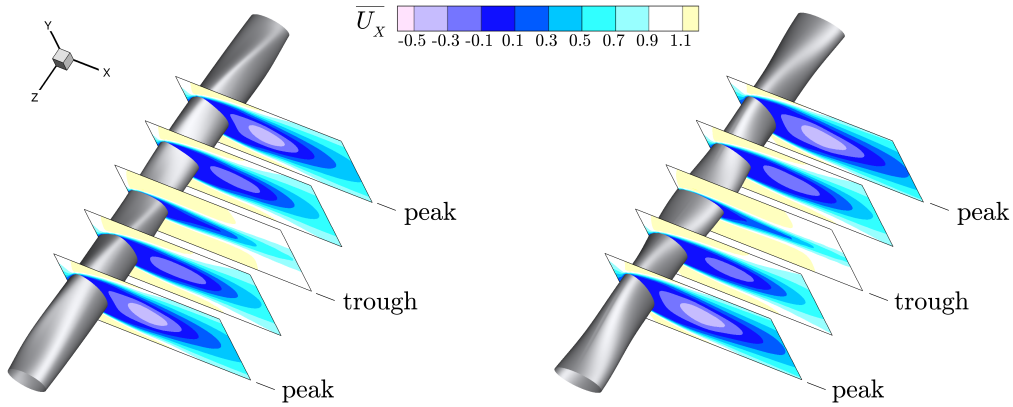

(a) The comparison of time-averaged streamwise velocity contours for low A_C (left) and high A_C (right) models shows a relative similarity between the two models. Contours are shown at equally spaced spanwise locations where peak and trough correspond to A_T undulations.

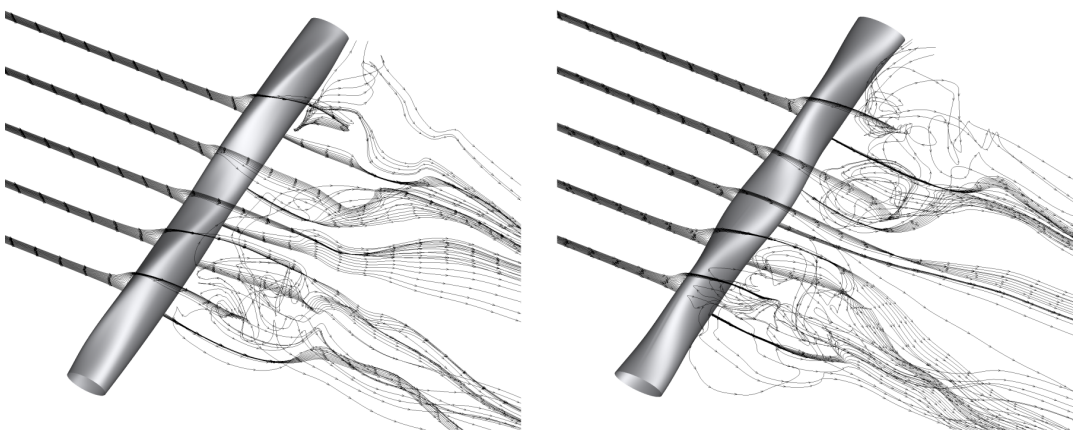

(b) Velocity streamlines at peak and trough spanwise locations denoted in 9a demonstrate the similarity in the streamwise flow component and a modest increase in spanwise flow for the high A_C model.

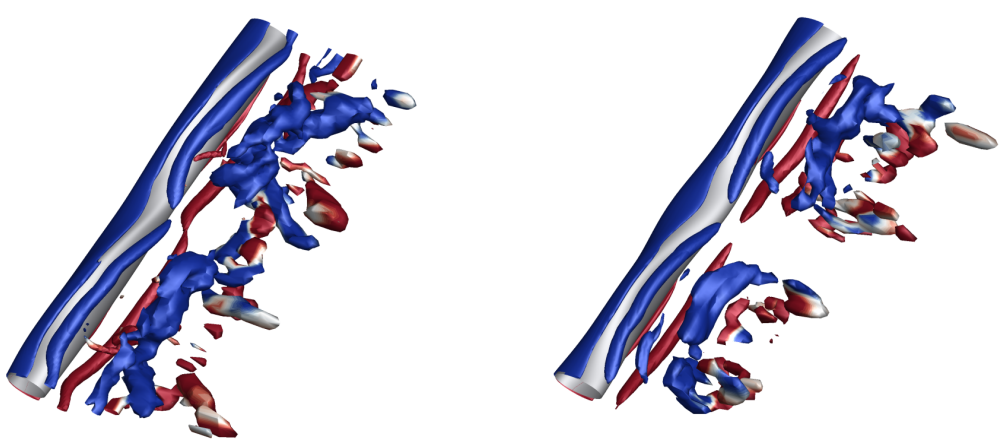

(c) Isosurfaces of Q-criterion colored by spanwise vorticity display a considerable break towards the center of the high A_C model.

Figure 9: Flow comparison between low and high A_C geometries. CL2 (low A_C) in the left column, CL4 (high A_C) in the right column.

parameter as previously discussed. However, differences are seen in the Q-criterion isosurfaces in figure 9c where the high A_C geometry has no coherent vortex structure in the center of the span where the chord length is the largest. The local, more elliptical, cross-section mitigates flow separation in the center of the span, thus reducing drag and lift fluctuations as A_C is increased. The effect of increasing A_C has a larger impact on circular aspect ratio models. For these geometries, the change in the chord length due to the high A_C value in table 2 represents a larger percent of the overall chord length than for elliptical aspect ratio models.

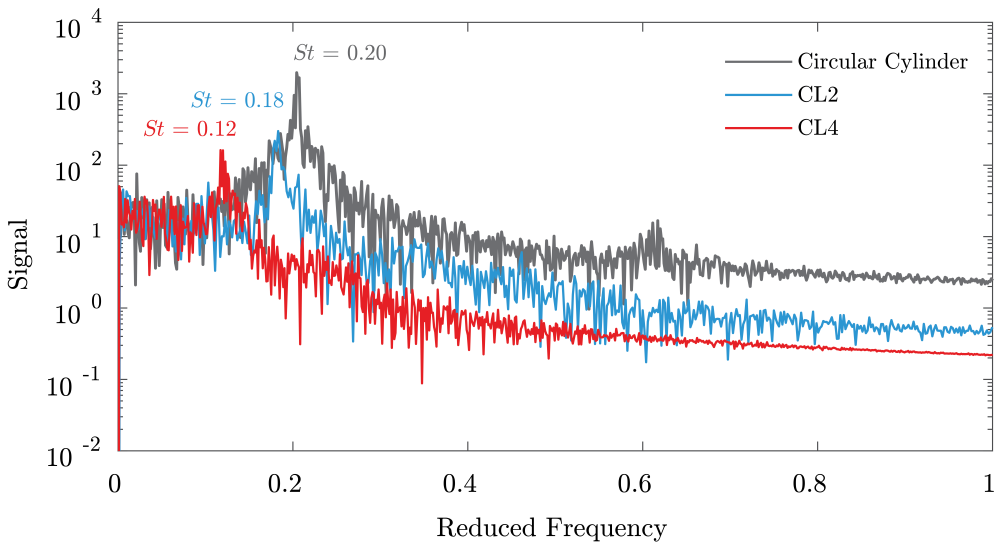

Figure 10: C_L spectra for the CL2 (low A_C) and CL4 (high A_C) geometries shown in figure 8 directly compared with a smooth circular cylinder. A gradual decrease in St occurs as A_C increases.

The spectra for CL2 and CL4 shown in figure 10 show that the intermittent spanwise features are correlated with a shift to lower frequencies and lower amplitudes. The smooth circular cylinder has the strongest and highest frequency peak, that gradually shifts to $St = 0.18$ for low A_C and to $St = 0.12$ for high A_C. Moreover, the high A_C model has reduced amplitudes at $f^* > 0.6$ and an overall lower magnitude at $St = 0.12$, consistent with the reduction in $C_{L,RMS}$.

3.4. Effect of λ

Q-criterion isosurfaces for cases with low and high wavelength are presented in figure 11 for both circular and elliptical aspect ratio models and directly compared to smooth cylinders. The vortex structures shed from the low wavelength models take on the appearance of long spanwise coherent vortices, qualitatively similar to the smooth structures despite the large value of A_T. In contrast, the high λ case demonstrates more significant spanwise break up of the downstream vortex structures for both cross-sections.

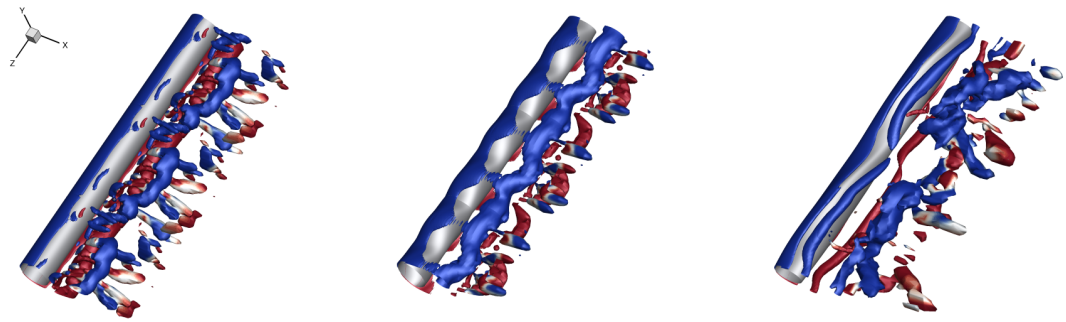

(a) Circular geometries (low γ). From left to right: no undulations, CS2 (low λ), CL2 (high λ).

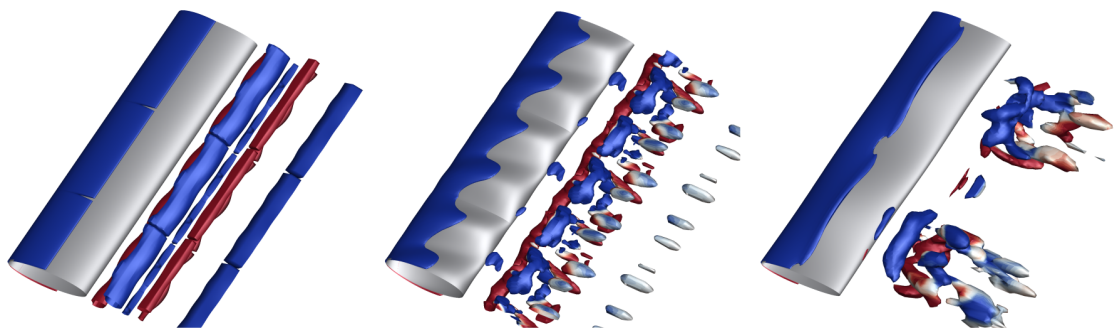

(b) Elliptical geometries (high γ). From left to right: no undulations, ES2 (low λ), EL2 (high λ).

Figure 11: Isosurfaces of Q-criterion colored by magnitude of spanwise vorticity show increased wavelength allows for break up of flow structures while flow structures from low λ models continue to resemble those of their smooth cylindrical counterparts.

In the C_L spectra shown in figure 12, the low λ cases have St peaks close to the frequency of their smooth cylinder counterparts, whereas the high λ cases have a significant decrease in St. Increasing the wavelength also increases the magnitude of the shift and decreases the amplitude of the peak, paralleling the reduction in $C_{L,RMS}$. The effect of the interaction $\lambda^* A_T$, noted in the St Pareto chart (figure 4c), is seen here. For high values of both λ and A_T, the reduction in St is greatly increased.

3.5. Effect of Undulation Offset (ϵ) and Symmetry (ϕ)

The effects of ϵ and ϕ are less prominent, and their impact is primarily overshadowed by the previously discussed geometric parameters. Nevertheless, the appearance of a large value of ϵ can incrementally decrease $\overline{C_D}$ and $C_{L,RMS}$. As streamwise flow travels along the chord length, the offset of the undulations increases the breakup of the spanwise structures, especially for geometries with a high and A_C value, although the interaction $A_C{}^*\epsilon$ is not specially computed. The impact of a other geometric parameters is thereby augmented by the high value of ϵ. The interaction $\lambda^*\epsilon$ is also shown to be important to both $\overline{C_D}$ and $C_{L,RMS}$. The complexity of this relationship is not fully understood and mostly likely results from the variety in flow induced by changes in wavelength.

Based on the current set of simulations, little quantitative data exists to support

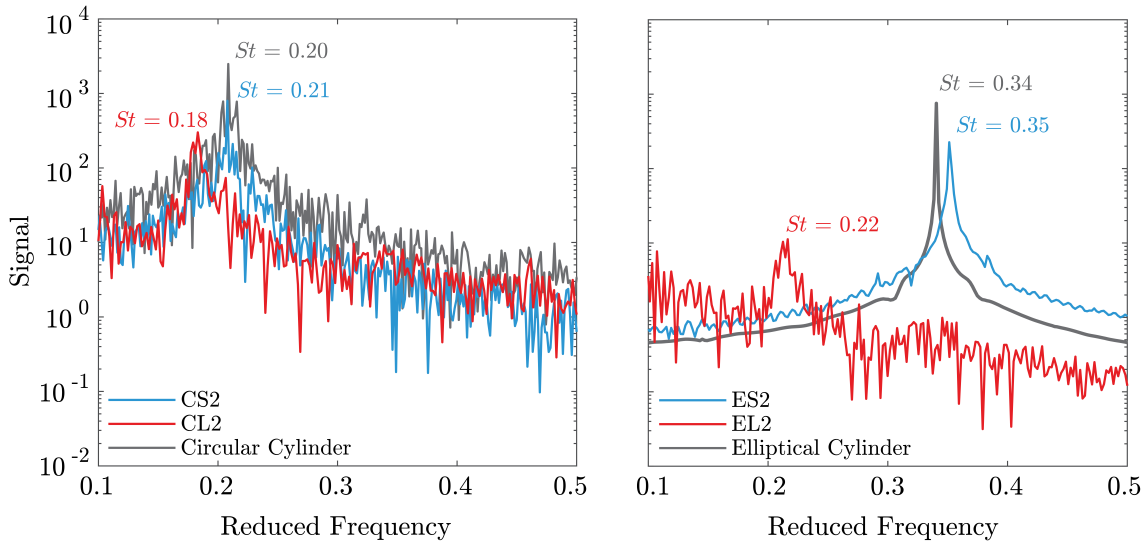

(a) Circular aspect ratio. (b) Elliptical aspect ratio.

Figure 12: Frequency spectra for low and high values of λ and γ compared with the smooth cylinder cases show St similarity between low λ and smooth models.

a correlation between ϕ and any of the calculated response variables. However, the parameter does impact the flow field and is most apparent for high A_C models. A high ϕ preferentially skews the spanwise velocity towards one direction as shown by model EL4 in figure 13. The model shown has a high value of A_T, A_C, ϵ, and ϕ. As discussed previously, a high A_T value results in significant momentum transport in the z-direction. The further addition of high ϵ and ϕ values result in this spanwise motion being directed nearly entirely in the negative z-direction. The asymmetry can be seen in the streamlines shown in figure 13c as well as the time-averaged z-velocity contour in figure 13d as the shed vortical structures tend towards the negative z-direction. Compared to model (EL2) with low values of A_C, ϵ, and ϕ, this model has a 3% reduction in $\overline{C_D}$, which is an incremental decrease compared with an already low-drag configuration.

4. Discussion

Unique to the seal whisker geometry is the combination of thickness undulations and chord length undulations. Consistent with the findings of Hans et al. [14], the magnitudes of both of these undulations, A_T and A_C, are shown to reduce $C_{L,RMS}$. A_T also significantly influences the frequency response, shifting the St to lower values for high A_T geometries. The current data show that an increase in A_T alone is capable of shifting St to lower frequencies and lower amplitudes by breaking up the strong coherent vortex structures characteristic of smooth surface cylinders. This vortex break up is explained by an increase in spanwise flow velocity at peak thickness locations, resulting in a subsequent decrease in oscillatory transverse flow and a reduction in $C_{L,RMS}$.

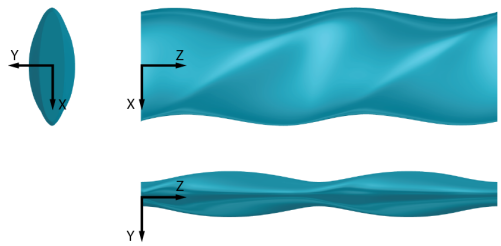

(a) EL4 (high ϵ and high ϕ): top view in the x-z plane, front view in the y-z plane, and side view in the x-y plane.

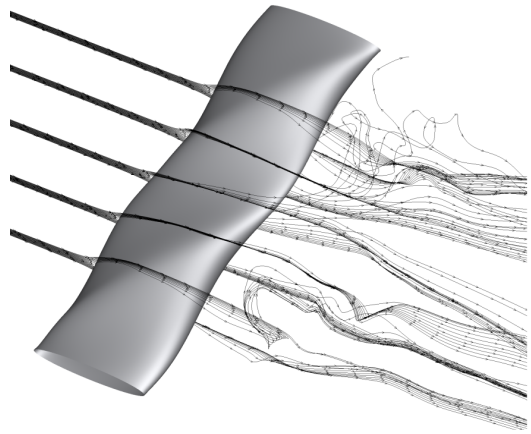

(b) Velocity streamlines at equally spaced spanwise locations as described in figure 9.

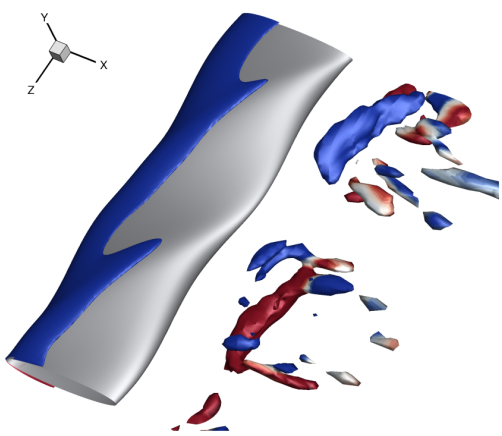

(c) Q-criterion isosurfaces colored by z-vorticity.

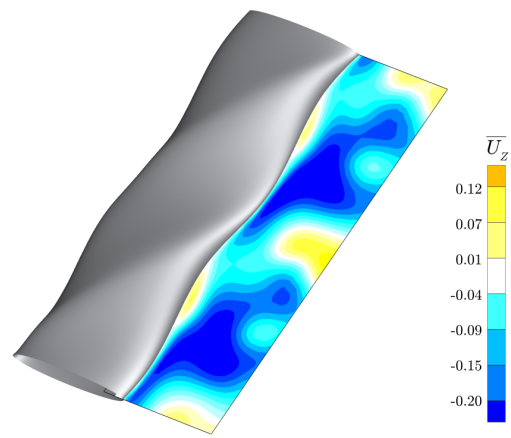

(d) Mean spanwise velocity in x-z plane.

Figure 13: Flow visualization for high ϕ and ϵ geometry reveals disjointed vortex structures and a preferential direction for the spanwise velocity.

Increasing A_C also reduces oscillations in lift, however through a different mechanism. A high A_C value creates cross-sections of varying chord lengths along the span, and thus the flow remains attached at locations of maximum chord length, significantly impacting the local drag for that portion of the span. Although the streamlines still separate dramatically on spanwise portions with more circular cross-sections, the regions of attached flow drive down both $C_{L,RMS}$ as well as $\overline{C_D}$.

Indeed, the current results suggest that A_C more strongly influences the drag response than A_T does. This result differs from the observations of Hans et al., who report that thickness undulations have a higher impact on drag than chord length undulations [14]. The discrepancy is likely due to different geometric testing methodologies. Hans et al. chose to eliminate one direction of undulation at a time, whereas the current method draws conclusions from a set including a low and a high value of each amplitude. Both methodologies only examine a small portion of the

parameter space in terms of amplitudes, and there are certainly regimes and subtleties that are not fully captured and are worthy of future investigation.

The periodicity of the seal whisker geometry is prescribed by the wavelength, λ, that governs the frequency of both undulations. The data demonstrates the strong relationship between the flow physics and the wavelength, λ, as it has a significant effect on all the response values investigated. The wavelength has been shown to have specific regimes of different flow responses in previous investigations of simpler wavy cylinders (single undulation in all directions) [23]. The different behavior between the low and high wavelength models of the simulation matrix indicate that these regimes may persist in the more complex undulations of the seal whisker model. Whereas the low λ models maintain coherent spanwise vortex structures as they are shed from the surface, the high λ models demonstrate a more complex vortex topology and a significantly different frequency response for the unsteady lift force.

Recent work completed by Liu et al. on seal whisker models also indicates a relationship between wavelength and varying flow regimes [15]. The results presented here, however, include effects of other geometric parameters and suggest an optimal wavelength below which other undulation parameters have limited effect on the flow response. Still, due to the small number of wavelengths tested, the full flow regime map resulting from wavelength changes in the seal whisker topology remains to be determined.

The final two geometric parameters, ϵ and ϕ, govern the symmetry of the seal whisker geometry. The effect of these geometric parameters are closely related to the inclination angles of the two ellipses, α and β, introduced by the original seal whisker model (figure 1a). These angles have shown high variability in seal whisker sample measurements and thus have been eliminated from various computational models [12, 15] as insignificant. Hans et al. show the angles α and β to have relatively little effect on the oscillatory response. However, when α and β are decreased, the undulation amplitudes also increase, as the two parameters are coupled. Thus, the novelty of the new geometric definitions introduced in this paper is that the geometric asymmetry parameters ϵ and ϕ (shown in figure 2) can both be modified independently from one another and the two amplitudes. Thus, this investigation can more accurately isolate the dependence of these parameters.

The data indicates that ϵ is more important than ϕ for all the response parameters, or the undulation offset between leading and trailing edge has a larger impact on the flow response than the symmetry of the undulations. Especially for models with high values of A_C, a high value of ϵ can incrementally decrease both $\overline{C_D}$, $C_{L,RMS}$. Interactions between λ and ϵ are also contributing to the force parameters and may be pursued in more detailed studies. The parameter ϕ has relatively little effect on all three response variables.

5. Conclusions

The complex topology of the harbor seal whisker is modeled with seven independent geometry parameters whose effects on response variables $\overline{C_D}$, $C_{L,RMS}$, and St are systematically tested. A simulation matrix of 16 seal whisker models, comprised of unique non-dimensional geometric parameter combinations is created using a two-level fractional factorial design of experiments. By applying large changes in the independent geometric parameters, the parameters that have the most significant impact on $\overline{C_D}$, $C_{L,RMS}$, and St are identified as γ, A_C, A_T, and λ. The flow physics associated with low and high values of each of these parameters are discussed in detail.

The effects of all the geometric parameters, summarized in figure 4, are designed to be a preliminary screening tool for more in-depth investigations. The initial flow analyses performed here does indicate specific trends supported by the flow physics, and isolate the dominant geometric features that most influence those trends. These findings are instrumental for bio-inspired design of a variety of structures, small and large, in which drag reduction, vibration suppression, and/or frequency tuning is required. Further research may investigate the effect of other geometric interaction and will likely focus on the optimal range of each of the significant parameters for various implementations.

The impact of understanding the physical response to geometric variations will also be of importance to the biological community. By exaggerating the physical characteristics of the seal whisker beyond that which is observed in nature, we can better identify the importance of morphology and provide context for the natural variation observed within and between species. In future work, a focused study across species may lead to insight into how whisker morphology impacts foraging and prey specialization.

Acknowledgements

The authors kindly thank Mr. Andrew Guarendi for his assistance in the simulations, and Prof. Kenny Breuer for providing laboratory space. JAF acknowledges funding from the ONR Summer Faculty Research Program and KL from the Naval Research Enterprise Internship Program (NREIP). This research was conducted using computational resources and services at the Center for Computation and Visualization, Brown University.

Distribution Statement A: Approved for public release. Distribution is unlimited.

References

[1] Dehnhardt G, Mauck B, Hanke W, Bleckmann H. 2001 Hydrodynamic Trail-Following in Harbor Seals (Phoca vitulina). *Science* **293**, 102–104.

[2] Hanke W, Witte M, Miersch L, Brede M, Oeffner J, Michael M, Hanke F, Leder A, Dehnhardt G. 2010 Harbor seal vibrissa morphology suppresses vortex-induced vibrations. *Journal of Experimental Biology* **213**, 2665–2672.

[3] Schulte-Pelkum N, Wieskotten S, Hanke W, Dehnhardt G, Mauck B. 2007 Tracking of biogenic hydrodynamic trails in harbour seals (Phoca vitulina). *Journal of Experimental Biology* **210**, 781–787.

[4] Wieskotten S, Mauck B, Miersch L, Dehnhardt G, Hanke W. 2011 Hydrodynamic discrimination of wakes caused by objects of different size or shape in a harbour seal (Phoca vitulina). *Journal of Experimental Biology* **214**, 1922–1930.

[5] Murphy CT, Reichmuth C, Mann D. 2015 Vibrissal sensitivity in a harbor seal (Phoca vitulina). *Journal of Experimental Biology* **218**, 2463–2471.

[6] Murphy CT, Reichmuth C, Eberhardt WC, Calhoun BH, Mann DA. 2017 Seal Whiskers Vibrate Over Broad Frequencies During Hydrodynamic Tracking. *Scientific Reports* **7**.

[7] Murphy CT, Eberhardt WC, Calhoun BH, Mann KA, Mann DA. 2013 Effect of Angle on Flow-Induced Vibrations of Pinniped Vibrissae. *PLOS ONE* **8**.

[8] Wang S, Liu Y. 2016 Wake dynamics behind a seal-vibrissa-shaped cylinder: a comparative study by time-resolved particle velocimetry measurements. *Experiments in Fluids* **57**.

[9] Wang S, Liu YZ. 2017 Flow structures behind a vibrissa-shaped cylinder at different angles of attack: Complication on vortex-induced vibration. *International Journal of Heat and Fluid Flow* **68**, 31–52.

[10] Kim H, Yoon HS. 2017 Effect of the orientation of the harbor seal vibrissa based biomimetic cylinder on hydrodynamic forces and vortex induced frequency. *AIP Advances* **7**.

[11] Morrison HE, Brede M, Dehnhardt G, Leder A. 2016 Simulating the flow and trail following capabilities of harbour seal vibrissae with the Lattice Boltzmann Method. *Journal of Computational Science* **17**, 394–402.

[12] Witte M, Hanke W, Wieskotten S, Miersch L, Brede M, Dehnhardt G, Leder A. 2012 On the Wake Flow Dynamics behind Harbor Seal Vibrissae – A Fluid Mechanical Explanation for an Extraordinary Capability. In Tropea C, Bleckmann H, editors, *Results of the DFG Priority Programme 1207 Nature-inspired Fluid Mechanics 2006-2012* , pp. 271–289. Berlin, Heidelberg: Springer.

[13] Rinehart A, Shyam V, Zhang W. 2017 Characterization of seal whisker morphology: implications for whisker-inspired flow control applications. *Bioinspiration & Biomimetics* **12**.

[14] Hans H, Miao J, Weymouth G, Triantafyllou M. 2013 Whisker-like geometries and their force reduction properties. In *2013 MTS/IEEE OCEANS - Bergen, Norway* pp. 1–7.

[15] Liu G, Xue Q, Zheng X. 2019 Phase-difference on seal whisker surface induces hairpin vortices in the wake to suppress force oscillation. *Bioinspiration & Biomimetics* **14**.

[16] Ginter CC, Fish FE, Marshall CD. 2010 Morphological analysis of the bumpy profile of phocid vibrissae. *Marine Mammal Science* **26**, 733–743.

[17] Ginter CC, DeWitt TJ, Fish FE, Marshall CD. 2012 Fused Traditional and Geometric Morphometrics Demonstrate Pinniped Whisker Diversity. *PLOS ONE* **7**.

[18] Jung UH, Kim JH, Kim JH, Park CH, Jun SO, Choi YS. 2016 Optimum design of diffuser in a small high-speed centrifugal fan using CFD & DOE. *Journal of Mechanical Science and Technology* **30**, 1171–1184.

[19] Beem H, Hildner M, Triantafyllou M. 2013 Calibration and validation of a harbor seal whisker-inspired flow sensor. *Smart Materials and Structures* **22**.

[20] Beem HR, Triantafyllou MS. 2015 Wake-induced slaloming response explains exquisite sensitivity of seal whisker-like sensors. *Journal of Fluid Mechanics* **783**, 306–322.

[21] Mason RL, Gunst RF, Hess JL. 2003 *Statistical Design and Analysis of Experiments with Applications to Engineering and Science* vol. 2nd ed *Wiley Series in Probability and Statistics*. New York: Wiley-Interscience.

[22] Antony J, Antony J. 2003 *Design of Experiments for Engineers and Scientists*. Jordan Hill, United Kingdom: Elsevier.

[23] Lam K, Lin YF. 2009 Effects of wavelength and amplitude of a wavy cylinder in cross-flow at low Reynolds numbers. *Journal of Fluid Mechanics* **620**, 195–220.

[24] Deardorff JW. 1970 A numerical study of three-dimensional turbulent channel flow at large Reynolds numbers. *Journal of Fluid Mechanics* **41**, 453–480.

[25] Weller HG, Tabor G, Jasak H, Fureby C. 1998 A tensorial approach to computational continuum mechanics using object-oriented techniques. *Computers in Physics* **12**, 620–631.